Insights into Spatio-temporal dynamics during shock – droplet flame interaction

Gautham Vadlamudi [1], Akhil Aravind [1], Saini Jatin Rao [1], and Saptarshi Basu [1,2]*

*: Corresponding author email: sbasu@iisc.ac.in

Affiliations:

[1] Department of Mechanical Engineering, Indian Institute of Science, Bangalore 560012, India

[2] Interdisciplinary Centre for Energy Research (ICER), Indian Institute of Science, Bangalore 560012, India

1. Shock Arrival time theoretical vs experimental

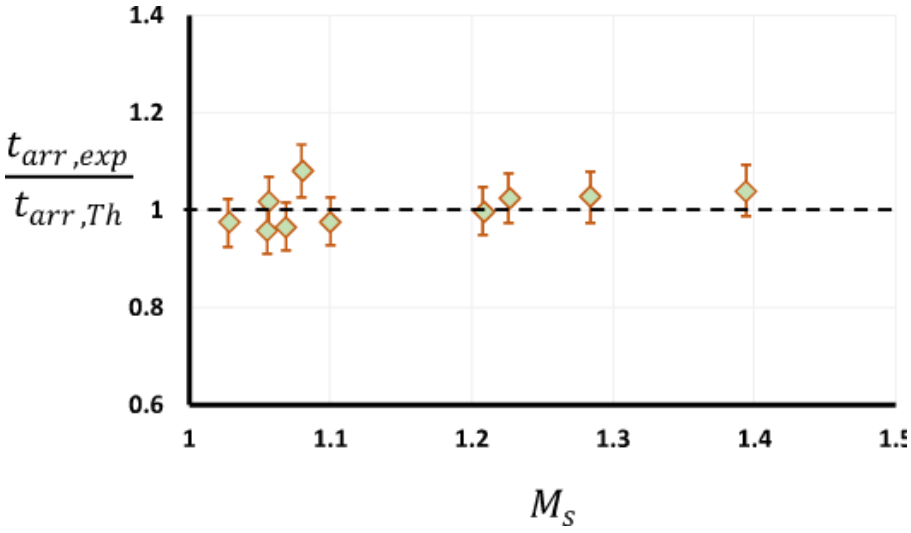

Figure S1. The ratio of experimentally obtained shock arrival time at the droplet location ($t_{arr,exp}$) to the theoretically estimated shock arrival time at the droplet location ($t_{arr,Th}$) is plotted against the corresponding shock Mach number.

The shock arrival time at the droplet location obtained from experiments ($t_{arr,exp}$) i

The shock arrival time at the droplet location is obtained theoretically ($t_{arr,Th}$) using Equation 3.11 in main manuscript, by substituting the characteristic length scale (R_o) that has been obtained by iteratively matching the theoretical estimate of shock Mach number (M_s) at the droplet location (Bach and Lee 1970) to the experimental value. The plot in Figure S1 shows that the shock arrival time of current experiments is in good agreement with the theory.

2. **Temporal pressure variation showing the time scale (t_d) which is used to obtain normalized time**

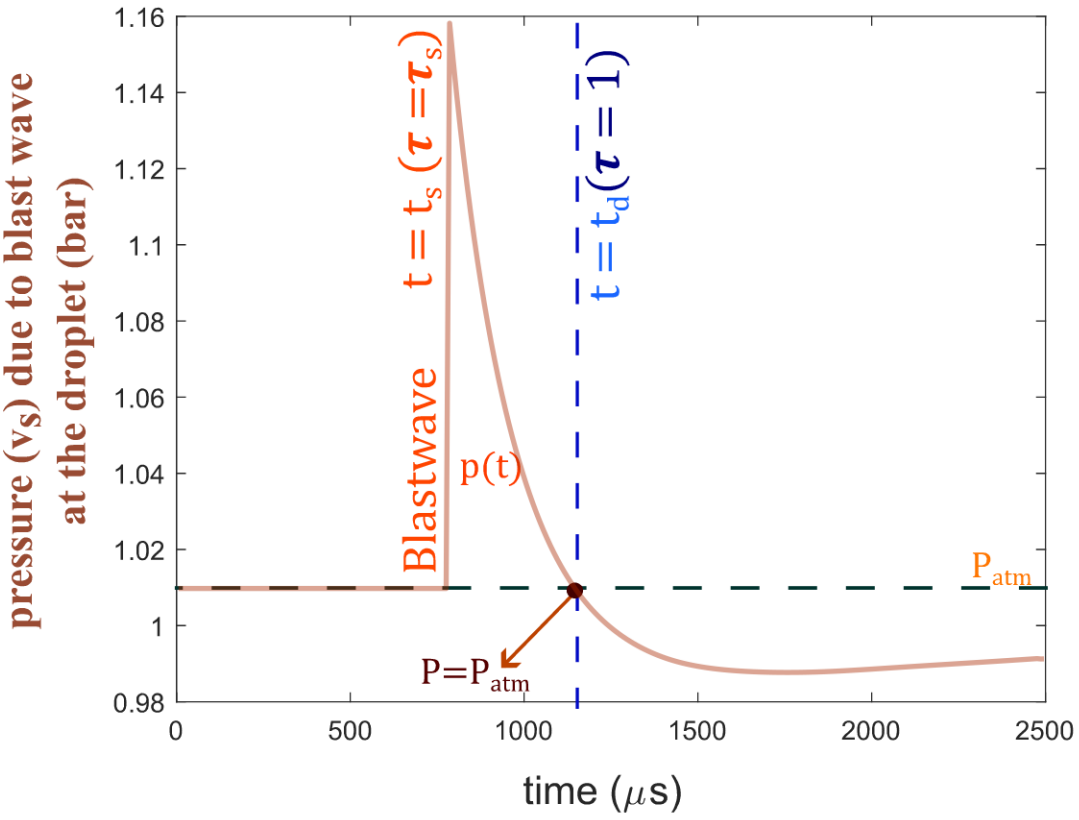

Figure S2. The theoretically obtained pressure variation at the droplet location with respect to time are plotted. t = 0 corresponds to the instant of explosion and t = t_s represents the time instant the blast wave reaches the droplet location for 10kV_Open case (M_s ~ 1.065). The time instant where the decaying pressure at the droplet location reaches atmospheric pressure (P_{atm}) is denoted by t = t_d.

The induced flow (v_{ind}) due to the entrainment effects occurs due to the low pressure ($P < P_{atm}$) developed locally, behind the blast wave, the time scale at which the local pressure decays below the ambient (P_{atm}) i.e., t_d is relevant to determine the two stages of interaction: interaction with the blast wave profile velocity (v_s) and interaction with the induced flow (v_{ind}). Thus, the time from explosion is normalized using the time scale 't_d' and the dimensionless time is given by:

$$\tau = \frac{t}{t_d}$$

This dimensionless time (τ) becomes unity when the local pressure at the droplet decays and reaches P_{atm} and induced flow (v_{ind}) is only observed for $\tau > 1$ and thus, for $\tau < 1$, only velocity scale that affects is imposed on the droplet-flame is the decaying velocity profile of the blast wave (v_s). The induced flow velocity scale (v_{ind}) is observed to be significantly smaller compared to the shock velocity scales, which results in a time delay for the induced flow to reach the droplet location after the shock interaction (t = t_s). The induced flow velocity scale (v_{ind}) is observed to increase with increase in shock strength (M_s) and depending on the M_s, the induced flow reaches the droplet at different times and for open-field

configuration, the induced flow effects are observed after $\tau > 1.3$ and for focused cases ($M_s > 1.1$) the induced flow CVR reaches the droplet after $\tau > 1$.

3. Simultaneous Parallax Schlieren and Mie-Scattering flow visualisation:

It is to be noted that in all the experiments, the Schlieren imaging has been performed with the optical axis of the camera orthogonal to the plane of the shorter side of the rectangular shock tube channel. To get a better understanding of the vortical structures, simultaneous Schlieren and Mie-scattering flow visualisation are performed. The Schlieren is set up with the optical axis orthogonal to the shorter side of the shock tube channel but at some parallax to obtain a better view of the three-dimensional structure of the flow features. A laser sheet is aligned parallel to the shorter side of the shock tube channel passing through the central plane and a high-speed camera is mounted with its optical axis orthogonal to the laser sheet. Thus, the horizontal x-direction in all the imaging is parallel to the shorter side of the shock tube and the longer side of the shock tube is along the perpendicular to the plane of the image. Figure S4 (main manuscript) shows the time series of the CVR evolution obtained using simultaneous parallax Schlieren imaging and Mie-scattering flow visualisation at the central plane parallel to the shorter side of the shock tube. The parallax Schlieren imaging clearly shows that the vortex loop has three-dimensional deformation. Since, both the imaging are obtained simultaneously, the macro features and the three-dimensional orientation of the CVR can be understood from the parallax Schlieren whereas, the local flow features at the central plane which interacts with the droplet can be obtained for the Mie-scattering imaging (length of the longer side is far greater than the droplet flame width).

The schematic of the evolution of the 3D macro features of the CVR is shown in figure 9d (main manuscript). For all the cases, the vortex ring is observed to attain a saddle-like shape with the leading edge of the saddle shape originating from the shorter side of the shock tube (towards and away from the camera) whereas the lagging edge of the saddle-shape originating from the longer side of the shock tube. This is evident in the parallax Schlieren images in figure S4a (right, at 2.00 ms), where the vortex loop towards and away from the camera (near the centre of the frame) are leading ahead whereas the sharp pointy features on the either side (left and right) lag behind (figure 9f). The central vortex loop edges arise from the shorter edges of the shock tube exit present towards and away from the camera, whereas the steep pointy edges on the either side arise from the longer edges of the shock tube exit which is parallel to the optical axis of the camera. It is evident from the figure 9d, figure S4b that the central horizontal edges of the vortex loop arising from the front and rear shorter edges of the shock tube exit (towards and away from the camera, see figure S4b) is slanted on the either side and these slanted front and rear edges meet at two points on either side (that appears as the sharp nodes in the parallax Schlieren imaging, shown in figure S4b). Thus, these sharp nodes at the junction of the slanted edges on the either side of the saddle-shaped vortex loop (emerging from both the shorter sides of shock tube) are located on the central plane of the shock tube (parallel to the shorter edge of the shock tube, i.e., plane of the laser sheet). This vortex behaviour matches with the experimental observations reported before in literature by Zare-Behtash et al. (2008, 2009) who studied the vortex loop evolution exiting a non-symmetrical nozzle. They showed that the vortex loop does not expand along the major axis as much as it expands along the minor axis and the portion of the vortex loop generated from the shorter edge has greater velocity downstream leaving behind the vortex loop portion from the longer side. This is reflected in the current experiments where the vortex edges emerging from longer side are lagging compared to that emerging from the shorter side.

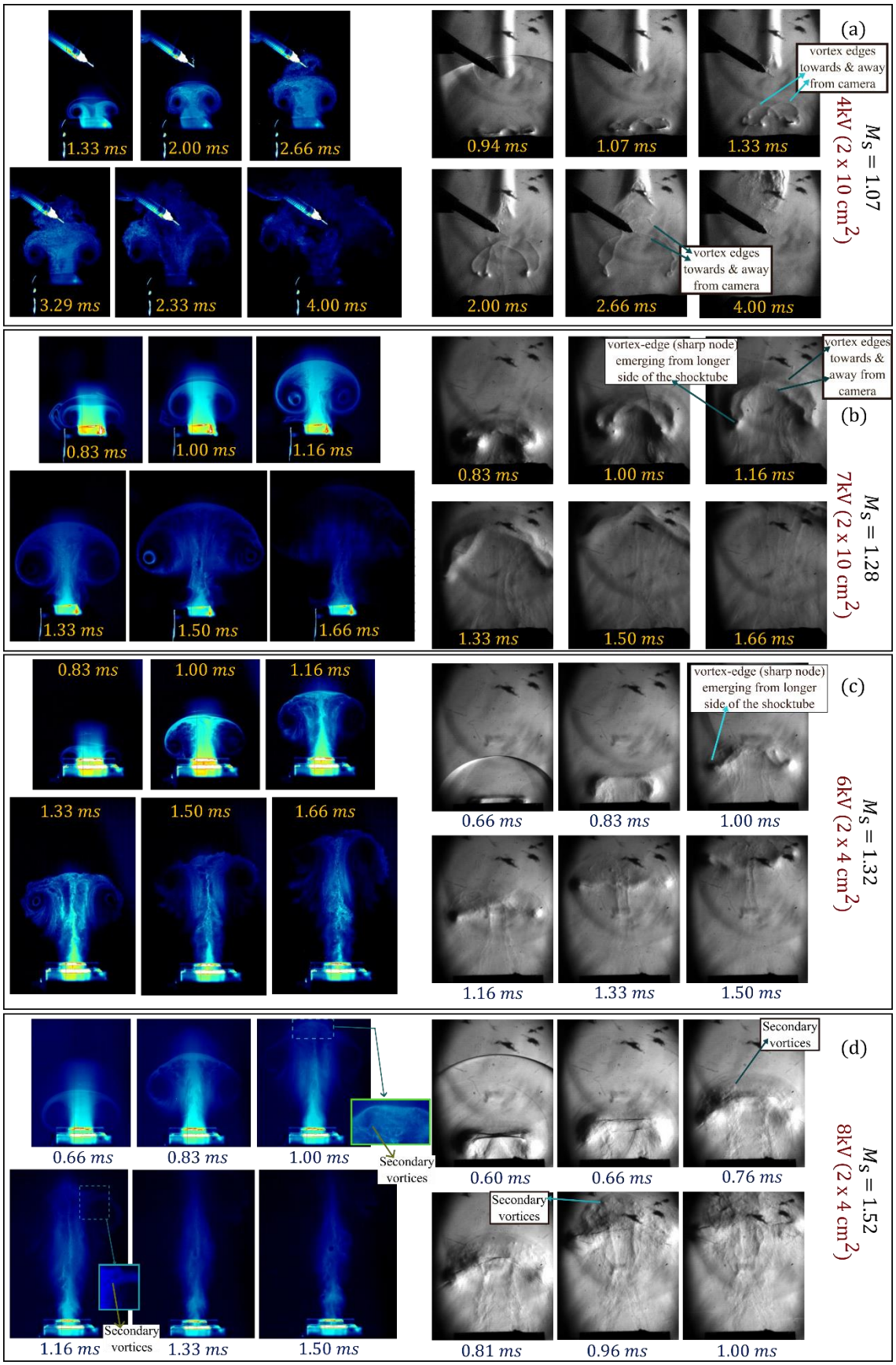
(a)
vortex edges towards & away from camera
4kV (2 x 10 cm^2)
M_S = 1.07
1.33 ms
2.00 ms
2.66 ms
3.29 ms
2.33 ms
4.00 ms
0.94 ms
1.07 ms
1.33 ms
2.00 ms
2.66 ms
4.00 ms
vortex edges towards & away from camera
(b)
vortex-edge (sharp node) emerging from longer side of the shocktube
vortex edges towards & away from camera
7kV (2 x 10 cm^2)
M_S = 1.28
0.83 ms
1.00 ms
1.16 ms
1.33 ms
1.50 ms
1.66 ms
(c)
vortex-edge (sharp node) emerging from longer side of the shocktube
6kV (2 x 4 cm^2)
M_S = 1.32
0.66 ms
0.83 ms
1.00 ms
1.16 ms
1.33 ms
1.50 ms
(d)
Secondary vortices
8kV (2 x 4 cm^2)
M_S = 1.52
0.66 ms
0.83 ms
1.00 ms
Secondary vortices
1.16 ms
Secondary vortices
1.33 ms
1.50 ms
0.60 ms
0.66 ms
0.76 ms
Secondary vortices
0.81 ms
0.96 ms
1.00 ms

Figure S4. Time series of the shock flow depicting the simultaneous planar Mie scattering flow visualisation at the central plane parallel to the shorter edge of the shock tube (left) and the parallax Schlieren imaging (right): for bigger channel (2 cm × 10 cm c/s) at the charging voltages: (a) 4kV_B, (b) 7kV_B and for smaller channel (2 cm × 4 cm c/s) at the charging voltages; (c) 6kV_S, (d) 8kV_S.

As shown in figure S4, when the input energy is increased for the wire-explosion, the CVR translation velocity increases. The saddle-like shape of the CVR and the CVR evolution pattern as depicted in figure 9d is observed in all the cases in the parallax Schlieren images shown in figure S4. The central plane Mie-scattering visualisation of the CVR shows a distinct, smooth boundary of the vortex structure without any instabilities till the case with M_s < 1.30. However, beyond M_s >1.30, the CVR boundary is observed to show KH instability-driven corrugations along the vortex boundary in the Mie-scattering imaging (figure S4e). At even higher energy input (8 kV), figure S4d (left) shows the presence of secondary vortices near the leading boundary of the CVR, that have formed due to the growth of KH instabilities.

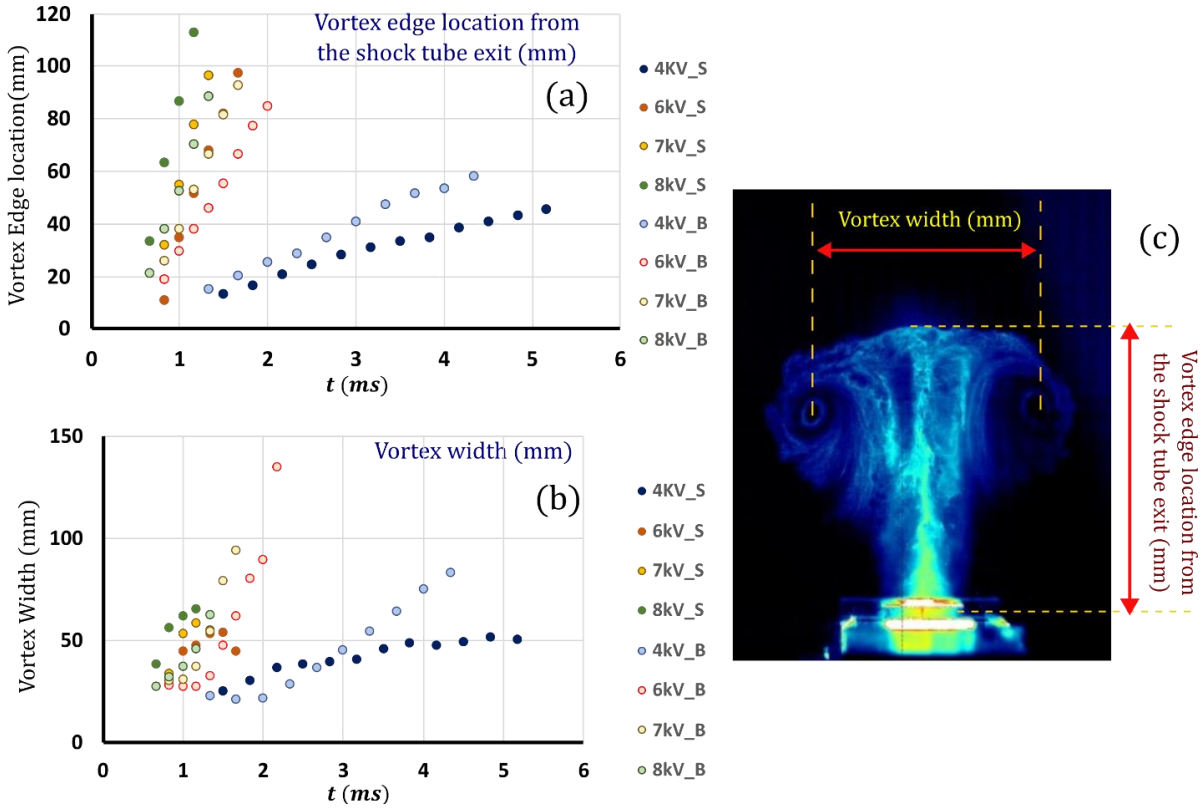

Figure S5. Plot of the temporal variation of the vortex (CVR) dimensions (mm): (a) vortex edge location and (b) vortex width (eye-to-eye distance) for all the cases of shock tube focusing. (c) Schematic showing the measurement of the dimensions of the CVR. Here, 'B' represents bigger channel (2 cm × 10 cm c/s), and 'S' represents smaller channel (2 cm × 4 cm c/s). Mie-scattering figure in 'c' corresponds to M_s = 1.32 (6kV_S case).

The pointy nodes in parallax Schlieren which are present on the central plane parallel to the shorter shock tube edge are tracked and are found to correspond with the vortex eyes that are observed in the planar Mie-scattering flow visualisation in the central same plane. Figure S5 shows the plots of the characterization of the vortical structures arising from the shock tube for different cases. The CVR edge and vortex eye locations were spatially tracked with time and the vortex edge location, eye-to-eye distance are plotted with time in figure S5 a,b. It shows that the vortex translational velocity increases with an increase in input

energy. It is observed that, the vortex width drastically increases after it exits the shock tube edge, and this expansion is more pronounced for lower charging voltages (4kV) as shown in figure S5b. The corresponding simultaneous parallax Schlieren imaging shows that the vortex loop is initially observed to be wound-up on the either side (see figure 9d), which gets unwound as the CVR propagates downstream away from the shock tube edge. It is observed that this unwinding phase corresponds to the rapid vortex expansion (increase in vortex width) that is observed in the planar vortex visualisation in the central plane. This unwinding of the vortex loop can also be clearly observed in figure 9f from 1.11 – 1.77 ms for 4kV charging using a smaller shock tube. This unwinding is also seen for higher charging voltages (see 0.8 – 1.16 ms in figure S4f), however, the expansion rate is not as prominent as the 4 kV charging case. The time series of simultaneous parallax Schlieren and Mie scattering flow visualisation with ignited droplet is shown in supplementary figure S3. It is to be noted that, since the amount of seeding and its distribution cannot be controlled (as explained in section 2), the Mie-scattering images are only used for evaluating the order of magnitude of the velocity scale associated with the vortex (v_{CVR}), which plays an important role in the droplet disintegration.

Simultaneous Mie scattering flow visualization and Parallax Schlieren for hot flow (with flame)

Figure S5 just shows the temporal evolution of the compressible vortex ring (CVR) exiting the shock tube. Figure S6 shows simultaneous parallax Schlieren and Mie-scattering imaging of the interaction of the CVR with the droplet flame. It can be clearly seen that the flame blowout already occurs in all the cases till the compressible vortex (CVR) starts to interact with the droplet flame. It is to be noted that for the Mie-scattering flow visualization, the seeding is introduced into the shock tube prior to the experiment and the seeding particles are observed to only exit the shock tube along with the CVR and not with the shock wave or the induced flow behind the shock wave. Furthermore, the Mie-scattering flow visualization is recorded using a high-speed camera by using a 10 μs exposure width of the laser sheet illumination sufficient to freeze the high-speed phenomena of the experiments. However, the camera recording is done at a lower acquisition rate (6000 fps) that corresponds to a larger exposure time in comparison with the shock flow time scales in current experiments. Thus, the features that are visible through the laser illumination scattering are frozen and captured at a very low exposure time, however, illuminating sources other than the synced laser such as the droplet flame will be captured at a longer exposure time corresponding to the acquisition rate, which results in motion blur for the flame visuals. This can be observed in the first few images in each case (before the vortex arrives) in figure S6, where the flame appears to be stretched to drastic lengths, however, that apparent elongation is a visual artifact of the motion blurring of the flame blowout phenomenon that occurs during the first stage of the interaction between shock wave ($\tau < 1$) and the droplet flame. This is also evident from the high-speed Schlieren and high-speed OH* Chemiluminescence imaging conducted at higher fps (smaller exposure times) that avoids motion blur. For $M_s > 1.1$, the flame is observed to blow out and fully extinguish before the CVR arrives at the droplet. Furthermore, the droplet breakup is primarily occurring during the interaction with the CVR which is evident from figure S6. It is also observed that after the droplet breakup the droplet spray cloud (daughter droplets) gets entrained in the CVR (compressible vortex ring). In addition to the Mie-scattering imaging which are obtained using single-pulse mode of the high-speed laser, the data has also been captured using the double-pulse laser with inter pulse spacing of 10 μs, which allows to record consecutive frames of the compressible vortex propagation with very small time-delay. Since uniform seeding of the shock tube flow is experimentally challenging due to its intrinsic transient nature, performing PIV algorithm on these consecutive frames could not give a detailed spatial flow-field. However, the order of magnitude of the velocity scale associated with the CVR along the centerline (where the droplet is located) can be obtained from the vectors generated using the PIV algorithm. These values are found to be of similar order as that of the CVR translational velocity that is obtained from the Schlieren imaging.

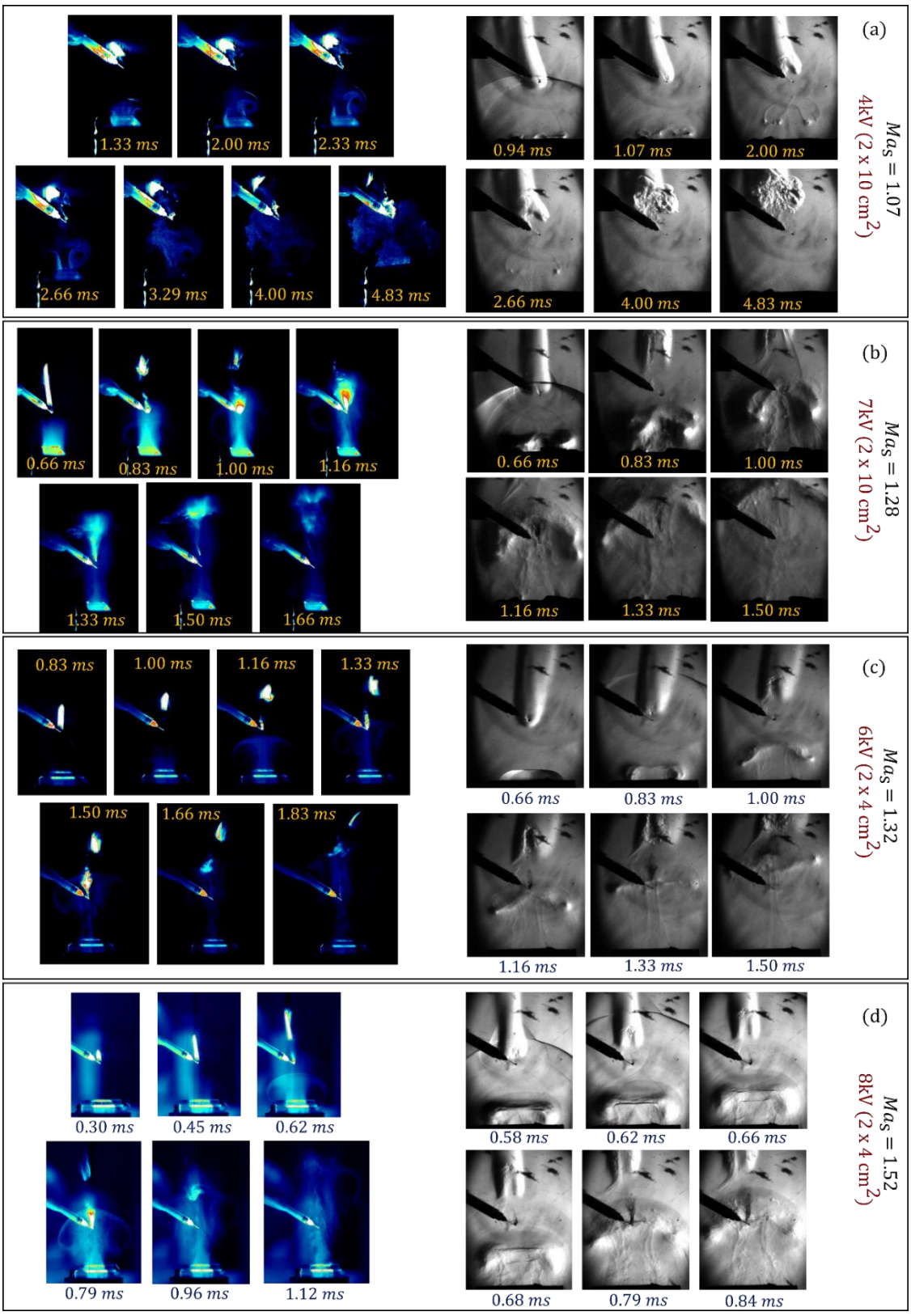

Figure S6. Time series of the interaction of the shock flow with the droplet flame, depicting the simultaneous planar Mie scattering flow visualization at the central plane parallel to the shorter edge of the

shock tube (left) and the parallax Schlieren imaging (right): for larger channel (2 cm × 10 cm c/s) at the charging voltages: (a) 4kV, (b) 7kV and for smaller channel (2 cm × 4 cm c/s) at the charging voltages; (c) 6kV, (d) 8kV.

Figure S7: Logic gate circuit to alter the clock-pulse signal from camera to have intermittent dim frame to simultaneously visualize the flame location and tip.

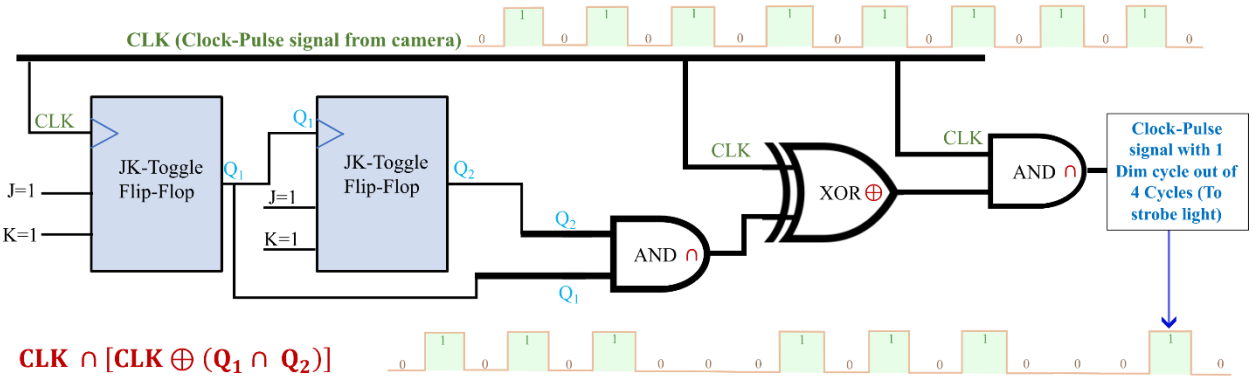

Figure S7 shows the Logic circuit used to convert the clock pulse signal from the camera (syncing) to intermittent dimming signal (1 out of 4 cycles is dim), to image the flame by making it better visible in the dark frame (no back light) to simultaneously get the flame location information during Schlieren imaging (for reference). This flame information is corroborated by the simultaneous high-speed OH* Chemiluminescence imaging to get better understanding about the flow around the flame along with the flame location and dimensions. The Logic circuit consists of two JK-type Toggle flip-flops (in series) and a combination of logic gates to obtain the desired signal.

References

Bach, G.G., Lee, J.H.S., 1970. An analytical solution for blast waves. AIAA J. 8, 271–275.

Zare-Behtash, H., Kontis, K., Gongora-Orozco, N., 2008. Experimental investigations of compressible vortex loops. Physics of Fluids 20, 126105.

Zare-Behtash, H., Kontis, K., Gongora-Orozco, N., Takayama, K., 2009. Compressible vortex loops: Effect of nozzle geometry. International Journal of Heat and Fluid Flow 30, 561–576.